CrossMark

Synchronous Rotation in the (136199) Eris–Dysnomia System

Gary M. Bernstein[1], Bryan J. Holler[2], Rosario Navarro-Escamilla[1], Pedro H. Bernardinelli[3,39], T. M. C. Abbott[4],
M. Aguena[5], S. Allam[6,40], O. Alves[7], F. Andrade-Oliveira[7], J. Annis[6], D. Bacon[8], D. Brooks[9], D. L. Burke[10,11],
A. Carnero Rosell[5,12,13], J. Carretero[14], L. N. da Costa[5], M. E. S. Pereira[15], J. De Vicente[16], S. Desai[17], P. Doel[9],
A. Drlica-Wagner[6,18,19], S. Everett[20], I. Ferrero[21], J. Frieman[6,19], J. García-Bellido[22], D. W. Gerdes[7,23], D. Gruen[24],
G. Gutierrez[6], K. Herner[6], S. R. Hinton[25], D. L. Hollowood[26], K. Honscheid[27,28], D. J. James[29], K. Kuehn[30,31],
N. Kuropatkin[6], J. L. Marshall[32], J. Mena-Fernández[16], R. Miquel[14,33], R. L. C. Ogando[34], A. Pieres[5,34],
A. A. Plazas Malagón[35], M. Raveri[36], K. Reil[11], E. Sanchez[16], I. Sevilla-Noarbe[16], M. Smith[37], M. Soares-Santos[7],
E. Suchyta[38], M. E. C. Swanson[37], and P. Wiseman[37]

(The DES Collaboration)

[1] Department of Physics and Astronomy, University of Pennsylvania, Philadelphia, PA 19104, USA; garyb@physics.upenn.edu
[2] Space Telescope Science Institute, Baltimore, MD 21218, USA
[3] DIRAC Institute and the Department of Astronomy, University of Washington, 3910 15th Avenue NE, Seattle, WA 98195, USA
[4] Cerro Tololo Inter-American Observatory, NSF's National Optical-Infrared Astronomy Research Laboratory, Casilla 603, La Serena, Chile
[5] Laboratório Interinstitucional de e-Astronomia—LIneA, Rua Gal. José Cristino 77, Rio de Janeiro, RJ—20921-400, Brazil
[6] Fermi National Accelerator Laboratory, P.O. Box 500, Batavia, IL 60510, USA
[7] Department of Physics, University of Michigan, Ann Arbor, MI 48109, USA
[8] Institute of Cosmology and Gravitation, University of Portsmouth, Portsmouth, PO1 3FX, UK
[9] Department of Physics & Astronomy, University College London, Gower Street, London, WC1E 6BT, UK
[10] Kavli Institute for Particle Astrophysics & Cosmology, P.O. Box 2450, Stanford University, Stanford, CA 94305, USA
[11] SLAC National Accelerator Laboratory, Menlo Park, CA 94025, USA
[12] Instituto de Astrofisica de Canarias, E-38205 La Laguna, Tenerife, Spain
[13] Universidad de La Laguna, Dpto. Astrofísica, E-38206 La Laguna, Tenerife, Spain
[14] Institut de Física d'Altes Energies (IFAE), The Barcelona Institute of Science and Technology, Campus UAB, E-08193 Bellaterra (Barcelona) Spain
[15] Hamburger Sternwarte, Universität Hamburg, Gojenbergsweg 112, D-21029 Hamburg, Germany
[16] Centro de Investigaciones Energéticas, Medioambientales y Tecnológicas (CIEMAT), Madrid, Spain
[17] Department of Physics, IIT Hyderabad, Kandi, Telangana 502285, India
[18] Department of Astronomy and Astrophysics, University of Chicago, Chicago, IL 60637, USA
[19] Kavli Institute for Cosmological Physics, University of Chicago, Chicago, IL 60637, USA
[20] Jet Propulsion Laboratory, California Institute of Technology, 4800 Oak Grove Drive, Pasadena, CA 91109, USA
[21] Institute of Theoretical Astrophysics, University of Oslo.P.O. Box 1029 Blindern, NO-0315 Oslo, Norway
[22] Instituto de Fisica Teorica UAM/CSIC, Universidad Autonoma de Madrid, E-28049 Madrid, Spain
[23] Department of Astronomy, University of Michigan, Ann Arbor, MI 48109, USA
[24] University Observatory, Faculty of Physics, Ludwig-Maximilians-Universität, Scheinerstr. 1, D-81679 Munich, Germany
[25] School of Mathematics and Physics, University of Queensland, Brisbane, QLD 4072, Australia
[26] Santa Cruz Institute for Particle Physics, Santa Cruz, CA 95064, USA
[27] Center for Cosmology and Astro-Particle Physics, The Ohio State University, Columbus, OH 43210, USA
[28] Department of Physics, The Ohio State University, Columbus, OH 43210, USA
[29] Center for Astrophysics | Harvard & Smithsonian, 60 Garden Street, Cambridge, MA 02138, USA
[30] Australian Astronomical Optics, Macquarie University, North Ryde, NSW 2113, Australia
[31] Lowell Observatory, 1400 Mars Hill Rd, Flagstaff, AZ 86001, USA
[32] George P. and Cynthia Woods Mitchell Institute for Fundamental Physics and Astronomy, and Department of Physics and Astronomy, Texas A&M University, College Station, TX 77843, USA
[33] Institució Catalana de Recerca i Estudis Avançats, E-08010 Barcelona, Spain
[34] Observatório Nacional, Rua Gal. José Cristino 77, Rio de Janeiro, RJ—20921-400, Brazil
[35] Department of Astrophysical Sciences, Princeton University, Peyton Hall, Princeton, NJ 08544, USA
[36] Department of Physics, University of Genova and INFN, Via Dodecaneso 33, I-16146, Genova, Italy
[37] School of Physics and Astronomy, University of Southampton, Southampton, SO17 1BJ, UK
[38] Computer Science and Mathematics Division, Oak Ridge National Laboratory, Oak Ridge, TN 37831, USA

Abstract

We combine photometry of Eris from a 6 month campaign on the Palomar 60 inch telescope in 2015, a 1 month Hubble Space Telescope WFC3 campaign in 2018, and Dark Energy Survey data spanning 2013–2018 to determine a light curve of definitive period 15.771 ± 0.008 days (1σ formal uncertainties), with nearly sinusoidal shape and peak-to-peak flux variation of 3%. This is consistent at part-per-thousand precision with the $P = 15.785\,90 \pm 0.00005$ day sidereal period of Dysnomia's orbit around Eris, strengthening the recent detection

[39] DiRAC Postdoctoral Fellow.
[40] Deceased.

of synchronous rotation of Eris by Szakáts et al. with independent data. Photometry from Gaia are consistent with the same light curve. We detect a slope of 0.05 ± 0.01 mag per degree of Eris's brightness with respect to illumination phase averaged across g, V, and r bands, intermediate between Pluto's and Charon's values. Variations of 0.3 mag are detected in Dysnomia's brightness, plausibly consistent with a double-peaked light curve at the synchronous period. The synchronous rotation of Eris is consistent with simple tidal models initiated with a giant-impact origin of the binary, but is difficult to reconcile with gravitational capture of Dysnomia by Eris. The high albedo contrast between Eris and Dysnomia remains unexplained in the giant-impact scenario.

Unified Astronomy Thesaurus concepts: Trans-Neptunian objects (1705); Small Solar System bodies (1469); Tidal friction (1698); Dwarf planets (419); Asteroid rotation (2211)

Supporting material: machine-readable table

1. Introduction

The trans-Neptunian region of icy minor bodies beyond the orbit of Neptune contains a record of the chemical composition and early dynamical history of the solar system. The observed dynamical structure of the modern trans-Neptunian region is complex (e.g., Elliot et al. 2005; Gladman et al. 2008; Petit et al. 2011; Adams et al. 2014; Bannister et al. 2018; Bernardinelli et al. 2022) and appears to be the result of giant planet migration early in solar system history (e.g., Fernandez & Ip 1984; Gomes et al. 2005; Hahn & Malhotra 2005; Morbidelli et al. 2007; Walsh et al. 2011; Lawler et al. 2019). Debate surrounds the timing and mechanism of this migration, but there is no debate that this period was a chaotic one for the primordial Kuiper Belt. A large fraction of the original mass in this disk was lost to the inner solar system, the Oort Cloud, or interstellar space (e.g., Gomes et al. 2005; Dones et al. 2015; Malhotra 2019), and some of the surviving trans-Neptunian objects (TNOs) are members of binary or multiple systems (e.g., Noll et al. 2020). The existence of some of these binary and multiple systems could be due to interactions with objects perturbed onto crossing orbits by the migration of the giant planets.

Ten of the largest known TNOs with at least one known satellite all have small secondaries with respect to the primary and separations <100 primary radii. Conversely, ten of the smallest known TNOs with known satellites have components of comparable size and a majority are separated by >100 primary radii (Figure 1). This dichotomy suggests different formation mechanisms, of which three broad categories exist: capture, gravitational collapse, and giant impacts (e.g., Brunini & López 2020). The capture mechanism has been well studied (e.g., Goldreich et al. 2002; Weidenschilling 2002; Funato et al. 2004; Astakhov et al. 2005; Lee et al. 2007; Schlichting & Sari 2008; Kominami et al. 2011), but is not favored for the formation of small TNO binaries due to the preponderance of prograde orbits (Grundy et al. 2011, 2019), which is less likely to result from capture (Schlichting & Sari 2008), and the correlated colors of binary components (Benecchi et al. 2009). Instead, gravitational collapse by the streaming instability has gained traction due to its efficiency in creating binaries with equally sized components and a wide range of semimajor axes (Youdin & Goodman 2005; Johansen et al. 2009; Nesvorný et al. 2010; Simon et al. 2017; Li et al. 2018). The giant-impact mechanism is favored for the satellites of large TNOs (e.g., Canup 2005; Brown et al. 2006; Canup 2011), though capture (Goldreich et al. 2002) and the collision of two objects within the Hill sphere of a third (Weidenschilling 2002) are also potential options. Another potential formation mechanism is rotational fission, perhaps induced by collision, which has been

proposed in particular for the Haumea system (Ortiz et al. 2012; Noviello et al. 2022).

The origin of the most-massive TNO binary system, (136199) Eris and its satellite Dysnomia, is still under investigation. The giant impact and capture mechanisms are more likely options than the capture scenario, given that the Weidenschilling (2002) mechanism mentioned previously is applicable primarily to the formation of small satellites (Brunini & López 2020). The diameter of Dysnomia, (700 ± 115 km; Brown & Butler 2018), comparable diameter ratio of Eris/Dysnomia and Pluto/Charon (Figure 1), and Dysnomia's low-eccentricity ($e = 0.006\,2 \pm 0.0010$; Holler et al. 2021), prograde orbit all tend to favor a giant-impact origin. However, the long orbital period of Dysnomia of $15.785\,899 \pm 0.000050$ days (Holler et al. 2021); stark albedo contrast between the two components, $0.96^{+0.09}_{-0.04}$ for Eris (Sicardy et al. 2011) versus $0.04^{+0.02}_{-0.01}$ for Dysnomia (Brown & Butler 2018); and lack of information on Dysnomia's orbital inclination with respect to Eris's equatorial plane do not necessarily fit that paradigm.

In this work, we determine the rotation period of Eris in order to evaluate the tidal state of the system and understand its origins. Nearly two decades after its discovery, and despite being among the brightest TNOs, the literature still presents partial and conflicting determinations of Eris's rotation period. A wide range of rotation periods has been reported, as summarized atop Table 3 of Verbiscer et al. (2022): >5 days (Carraro et al. 2006); 3.55 hr (Lin et al. 2007); 13.69, 27.38, and 32.13 hr (Duffard et al. 2008); 25.92 hr (Roe et al. 2008); and synchronous with Dysnomia's orbit (Rabinowitz & Owainati 2014; Szakáts et al. 2023). Roe et al. (2008) identified a signal in their periodogram at ~15 days, but discounted its significance because their photometry was obtained over a time period only twice as long. The difficulty in determining Eris's period from its rotational light curve is that the amplitude of variation is very low, only ~3% (or 0.03 mag) peak-to-peak, and the period is long, such that accurate determination of the period requires high signal-to-noise ratio (S/N) and photometric calibration to accuracy better than 0.01 mag across months or years of observations. Furthermore, on this timescale the solar phase curve is important to consider when constructing periodograms from sparse data, even though Eris's solar phase varies from only 0°.1–0°.6.

To meet this challenge, we combine photometry from three different telescopes. In chronological order: the Dark Energy Survey (DES) made 10 sweeps across a 5000 deg^2 swath of southern sky in each of the g, r, i, z, and Y filters over the period 2013 August through 2019 February, using a large-format camera on the 4 m Blanco telescope at Cerro Tololo
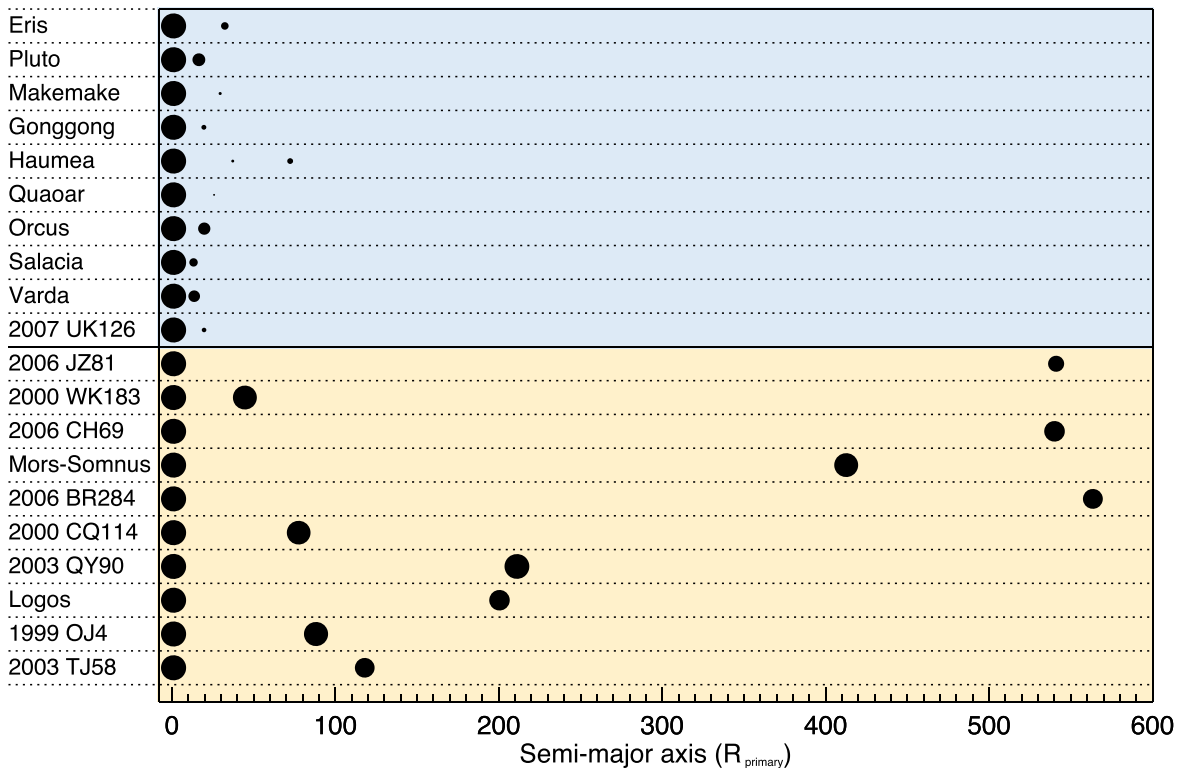
Figure 1. Each row depicts the size and separation of a TNO satellite relative to its primary body. Above the solid black line are shown 10 of the most-massive known binary systems, and 10 of the least massive are below, with all being ordered by primary mass. In general, larger TNO binaries present a larger size disparity between the components and tend to be on tighter orbits (in units of the primary radius, $R_{primary}$). Less-massive binaries are more widely separated, with comparably sized components. This dichotomy implies two different formation mechanisms for the two observed populations of TNO binaries. For Pluto, only Charon is shown due to the very small sizes of the minor satellites. System masses, semimajor axes, and component diameters were retrieved from the Johnston Archive (http://www.johnstonsarchive.net/astro/astmoontable.html) and references therein.

Interamerican Observatory (CTIO; Abbott et al. 2021). Usable images of Eris appeared in 8, 5, 6, and 7 exposures in the *griz* bands, respectively (*Y*-band images have insufficient S/N to be useful), out of the ~80,000 exposures of the DES Wide Survey. These exposures yield high S/N on Eris and benefit from the exquisitely accurate global photometric calibration of the survey (Burke et al. 2018). These measurements are, however, too sparse in time to determine an unambiguous period for Eris on their own.

The second set of data are a collection of nearly 1000 60 s exposures obtained between 2015 August and 2016 January in the Johnson *V* band with the "Facility Optical Camera" on the Palomar 60 inch (P60) robotic telescope (Cenko et al. 2006). Measures of useful S/N are obtained by averaging the exposures within each of the 72 nights. Their photometric quality is highly variable, but the DES imaging provides accurate reference magnitudes for objects in all of the P60 exposures. The more rapid cadence over a shorter time span is complementary to the sparse, long-term cadence of the DES data in determining an accurate period, and the two overlap in time.

The third set of data comprises images from the Hubble Space Telescope (HST) with the WFC3/UVIS instrument through the *F606W* filter on seven separate visits between 2018 January 1 and 2018 February 3 (GO program 15171, PI: B. Holler). These yield a very high S/N on Eris and easily resolve Dysnomia. While the time span of the HST data is too short to admit a precise determination of the photometric period, the high S/N and nonsidereal cadence of these data allow for a

more precise determination of the light curve and a veto on sidereal aliasing of the period.

As this work was being finalized, Szakáts et al. (2023) reported statistically significant candidate periods of 16.2 ± 0.5 days and 15.87 ± 0.22 days from a heterogeneous set of 31 nights of ground-based photometry spanning 15 yr and Gaia DR3 *G*-band photometry spanning 2.5 yr, respectively. Our results use a completely independent set of observations to test this assertion, and exploit higher-precision observations and increased sampling to exclude possible aliases and obtain a measurement of Eris's rotation period that is $10 \times$ more precise, as well as additional information on its phase curve and on Dysnomia's flux variations. We derive Eris's rotation period using data independent of Szakáts et al. (2023), and then incorporate the Gaia data into our final estimates of the light-curve parameters.

2. Observations and Data Reduction

2.1. Dark Energy Survey Images

The DES is a completed survey that covered ≈5000 square degrees of the southern sky using the Dark Energy Camera hosted at the Victor M. Blanco 4 m Telescope at CTIO in Chile. A full description of the DES observing sequences and calibration steps is given by Abbott et al. (2021), Morganson et al. (2018), and Burke et al. (2018). We note that the relative photometric zero-points of all of the accepted exposures in the survey are determined very well by solving for consistency among the tight web of overlapping exposures taken during the survey. Abbott et al. (2021) demonstrated rms differences of

Table 1
Photometric Data

MJD	Band	Exptime (s)	Phase (°)	Δ (au)	r (au)	Mag	Noise (mmag)	SysError (mmag)
56547.39494	g	90	0.344 1	95.63	96.45	19.086 9	4.7	3.0
56568.30048	g	90	0.182 3	95.49	96.45	19.048 0	4.5	3.0
56569.20107	g	90	0.176 5	95.49	96.45	19.048 4	4.1	3.0
56591.14610	g	90	0.170 4	95.49	96.44	19.069 1	4.6	3.0
56899.62065	G	40	0.449 2	95.69	96.39	18.611 4	13.2	…
56899.69466	G	40	0.448 7	95.69	96.39	18.593 1	13.9	…
56932.33489	r	90	0.191 0	95.43	96.38	18.492 5	3.5	3.0
…	…	…	…	…	…	…	…	…
58152.19177	F606W	348	0.549 7	96.49	96.15	18.843 3	2.2	3.0
58152.19766	F606W	348	0.549 7	96.49	96.15	18.844 1	2.3	3.0
58152.20492	F606W	585	0.549 7	96.49	96.15	18.834 6	1.8	3.0

Note. The photometric data used in determining Eris's light curve are given in temporal order. Magnitudes and MJDs are as observed, before corrections for distance and light-travel time. SysError is the amount added in quadrature to the measurement noise of each observation to account for calibration and other systematic errors. The *F606W* band is from HST, the *V* band is from the Palomar 60 inch (with exposures already averaged into ≈30 minute segments), g and r are from DES, and the *G* band is from Gaia. Table 2 is published in its entirety in machine-readable format. A portion is shown here for guidance regarding its form and content.

(This table is available in its entirety in machine-readable form.)

Table 2
HST Orbit-averaged Photometry

MJD	Phase (°)	Δ (au)	r (au)	Eris (mag)	Uncert. (mmag)	Dysnomia (mag)	Uncert. (mmag)
58119.28005	0.572 5	95.95	96.15	18.535 5	2.1	24.632	26
58119.47863	0.572 9	95.95	96.15	18.538 9	2.0	24.589	25
58121.25762	0.576 4	95.98	96.15	18.550 8	3.2	24.747	47
58127.22729	0.584 3	96.08	96.15	18.543 7	2.0	24.466	25
58128.41934	0.584 7	96.10	96.15	18.537 4	2.0	24.743	27
58132.45865	0.586 5	96.17	96.15	18.533 0	2.0	24.486	24
58152.19203	0.549 7	96.49	96.15	18.545 1	2.0	24.684	28

Note. Magnitudes of Eris and Dysnomia measured by HST/WFC3/UVIS in the *F606W* band. Each row is the combination of one HST orbit's exposures. Magnitudes and MJDs are as observed, before corrections for distance and light-travel time. Uncertainties include both measurement noise and estimated systematic contributions.

just 3 mmag between DES and Gaia stellar-source calibrations, implying that both surveys are calibrated to this level or better across the sky. All calibrated DES exposures, including those used herein to measure Eris, are part of the second public data release.[41]

We extract photometry for Eris from the 26 relevant images in 2013–2018 using the methods for moving-object photometry described by Bernardinelli et al. (2023). To summarize: photometric zero-points and a model of the (color-dependent) point-spread function (PSF) for each exposure are derived as part of the survey pipelines. We model a small region around each exposure of Eris jointly with the (typically) seven other DES exposures of that sky location in the same filter on different nights, when Eris was absent. The model consists of a free array of background sources that are assumed to exist in all exposures, plus a point source in Eris's location that is present only in a single exposure. This "scene-modeling photometry" yields shot-noise-limited photometry for Eris that is unaffected by potential overlapping background sources. Following Abbott et al. (2021), we add an additional 0.003 mag of uncertainty to each measured Eris magnitude to allow for local zero-point uncertainties. Resultant magnitudes for Eris are listed in Table 1.

At maximum elongation, Dysnomia is ∼500 mas from Eris (Brown & Schaller 2007; Brown & Butler 2018; Holler et al. 2021), so the ground-based DES (and P60) images did not

resolve Eris from Dysnomia. However, because Dysnomia's flux is 0.21% ± 0.01% that of Eris at $\lambda \approx 600$ nm (according to Brown & Schaller 2007; we find higher but still small ∼0.4% values in Table 2), any contamination of the DES or P60 light curves of Eris by variations in Dysnomia's magnitude must be at the submillimagnitude level in the g, r, and V bands. In the i and z bands of DES, the contribution of the redder Dysnomia could be much larger: Brown et al. (2006) reported Dysnomia to have 1.9% ± 0.5% of Eris's flux in the K' band.

2.2. Palomar 60 inch (P60) Telescope

The Palomar 60 inch (P60) telescope is a fully automated queue telescope that schedules observations in real time based on constraints for requested observations and sky conditions. In total, the Eris/Dysnomia system was observed by the P60 facility camera with the Johnson V filter in 1054 exposures across 72 nights between 2015 August 6 and 2016 January 29. Average seeing at the P60 is 1″.1 in the R band in the summer and 1″.6 in the winter. The facility camera had a 2k × 2k back-illuminated CCD detector and a field of view of 12″.9 × 12″.9 (Cenko et al. 2006). The facility camera has since been replaced with the SED Machine (Blagorodnova et al. 2018). Ultimately, 42 of the nights contained data that passed all quality cuts (i.e., adequate seeing, accurate pointing, photometric stability, etc.).

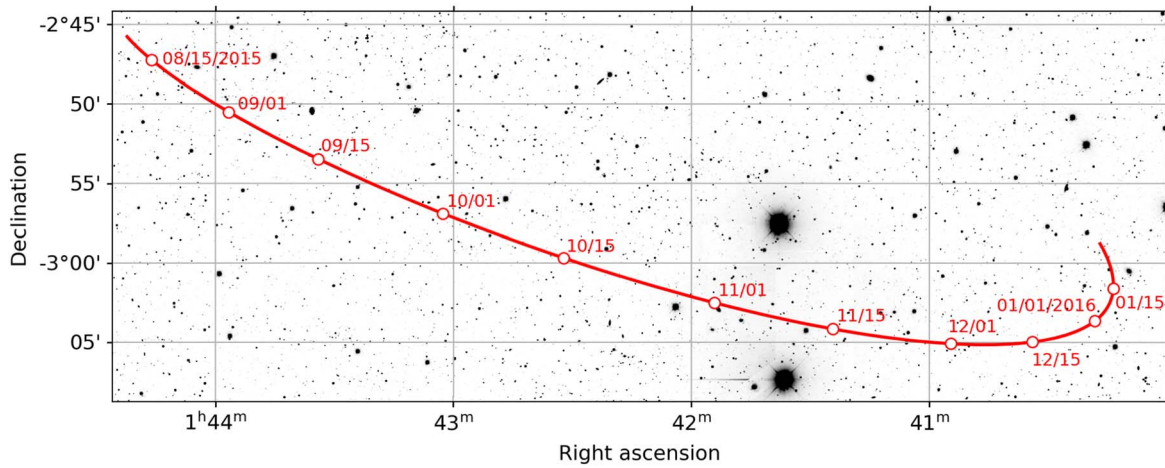A minimum of 12 1 minute images were requested each night. On some nights, additional sets of 12 images were

---
[41] https://des.ncsa.illinois.edu/releases/dr2

Figure 2. Position of Eris from 2015 August 6 to 2016 January 29 UT, retrieved from JPL Horizons, with 15 day intervals marked. The background is the coadded DES r-band image with a scale of $\sim 1''$ pixel^{-1}. For comparison, the full field of view of the P60 facility camera is $12\rlap{.}'9 \times 12\rlap{.}'9$ (Cenko et al. 2006).

obtained, but sometimes a sequence was partially or totally lost due to, e.g., a target-of-opportunity interruption or Eris being too near a bright star or detector defect. The track of Eris across the sky over this period is shown in Figure 2. The track is wholly contained within the DES survey footprint, and we use the summed DES image ("coadd") to confirm that a given sequence's images were not atop any other sources brighter than $r \approx 24$ mag. Fainter background sources might perturb one night's Eris photometry, but by <0.01 mag, which is comparable to the single-night statistical errors on P60 magnitudes.

Raw images were immediately processed through the P60 image analysis pipeline, which handled demosaicking, overscan subtraction, bias subtraction, flat-fielding with dome flats, sky-subtraction, bad-pixel masking, object detection, world coordinate system construction, and seeing and photometric zero-point estimation (Cenko et al. 2006). These processed data were then stored in an archive maintained by the Infrared Processing and Analysis Center.

Extracting fluxes accurate to <0.01 mag from the P60 data requires several steps of processing and quality control. First, we determine instrumental fluxes f and uncertainties σ for every star in every dome-flattened image via PSF fitting, as implemented by the codes PSFEX (Bertin 2011) and SEXTRACTOR (Bertin & Arnouts 1996). Measurements raising SEXTRACTOR error flags are discarded.

We identify detections of Eris by matching to its ephemeris, and the remaining P60 detections in each image are position-matched to stars in the DES coadd catalog (which is many times deeper than each P60 exposure). The DES g and r magnitudes of each match are recorded. We discard any exposure that does not match at least five DES stars with $0 < g - r < 1.3$ and S/N > 10.

The magnitude calibration process is done in batches of images from individual nights. We fit a zero-point $m_{0,i}$ for each image i and an overall color term c for the night to the matched stellar images using the measured fluxes f_{ij} in the V band and DES PSF_MAG_APER_8 magnitudes g_j, r_j for star j, via χ^2 minimization to the model:

$$
\begin{aligned}
m_{0,i} &- 2.5 \times \log_{10} f_{ij} \\
&= \tilde{V}_{\mathrm{DES},j} + c(g_j - r_j), \qquad \tilde{V}_{\mathrm{DES},j} \equiv (g_j + r_j)/2. \quad (1)
\end{aligned}
$$

The synthetic $\tilde{V}$ band created from DES fluxes is close to the native Johnson V band of the P60 data. We only use stars with $0 < g_j - r_j < 1.3$ for the photometric calibration. During the fitting process we add 0.003 mag of estimated flat-fielding error in quadrature to the σ_{ij} of individual stellar measurements, an amount chosen by eye to avoid over-weighting bright stars. Then we iteratively clip measurements that are >4σ away from the best fit.

We then fit the zero-points for each night's exposures to a model of linear dependence on airmass X:

$$
m_{0,i} = m_0 + k(X_i - 1), \qquad (2)
$$

iteratively clipping individual exposures having residuals to this fit that exceed 3× the rms variation of the night's residuals. We remove the clipped exposures from further consideration. We also drop the entire night's data if the rms deviation from the airmass law exceeds 0.04 mag. At this point we use the zero-points $m_{0,i}$ and the color term c to produce measured pseudo-V magnitudes,

$$
\tilde{V}_{ij} = m_{0,i} - 2.5 * \log_{10} f_{ij} - c(g_j - r_j), \qquad (3)
$$

for all surviving observations of Eris (taking $g - r = 0.518$ for Eris from DES data) and the reference stars. We use a constant color for Eris since our data do not detect any difference in the light curve between bands. Any phase-dependent color would result in magnitude shifts $\lesssim 1$ mmag. We next split the night's exposures into segments of time spanning at most 40 minutes, and for each source we average all of the measurements taken in that time period into a single measurement. We again perform sigma clipping to remove outliers caused by cosmic rays and other imaging defects. Most nights have only a single time segment. The output of the process is a catalog of time-averaged, calibrated $\tilde{V}$ magnitudes and their uncertainties for each source (including Eris), with both sky position and array position recorded, and the Julian date (JD) of the midpoint of each source's exposures.

At this point we must address a shortcoming of the P60 data reduction pipeline, which is the use of a dome flat to calibrate the response across the CCD. As emphasized in Bernstein et al. (2018), diffusely illuminated flat fields typically misrepresent
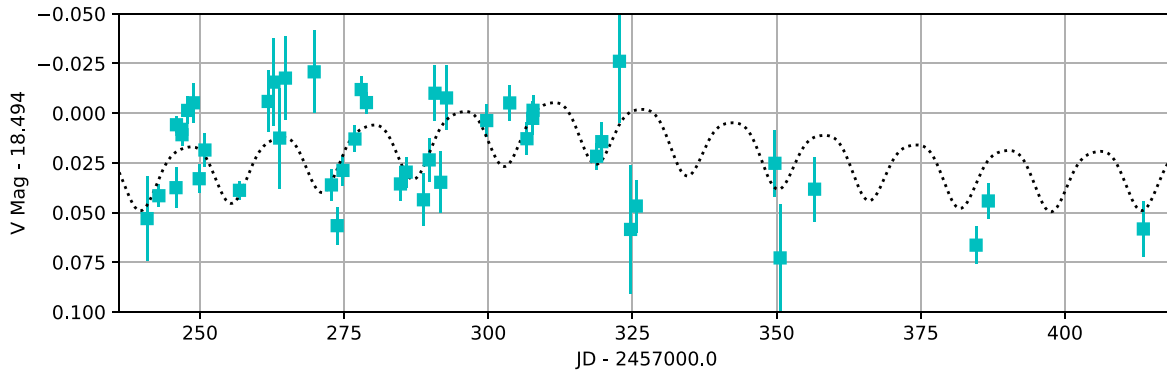
Figure 3. Time series of the P60 *V*-band measurements. The error bars are statistical only, and do not include calibration errors or systematics. The dotted curve is the model for synchronous rotation and the solar phase curve derived in Section 3.3. The periodicity is marginally visible in these unbinned data—see Figure 6 for phase-folded, binned versions. It is also clear that the phase variations produce a signal of comparable amplitude to the rotational light curve.

the camera's response to stellar illumination because the flat fields count both focused and scattered light, whereas stellar photometry uses only the properly focused photons. The resultant photometric errors depend on position on the detector array. This is a serious issue for Eris's light curve because the pointing of the P60 images was held fixed for several months at a time, meaning that Eris moved across the array while the reference stars stayed fixed at one position. Hence, the flat-field errors are translated directly into a spurious variation in Eris's brightness.

To correct for flat-field errors, we create a "star flat" by first tabulating the residual errors $\tilde{V}_j - \tilde{V}_{\mathrm{DES},j}$ between P60 and DES magnitudes for each measurement of each useful reference star. These residuals populate the (x,y) domain of the detector pixels irregularly. At each location on the detector, we set its star-flat value to the weighted mean of the eight nearest reference-star residuals to that location, with the weights given by a Gaussian function of the distance. The star-flat image for the P60 data varies by 5% across the detector, so these corrections are critical to obtaining useful light-curve data for Eris. We assume that the star-flat correction is constant for the entire Eris campaign, so we use all valid exposures' stellar photometry to create it.

The final step of the P60 photometry is to return to the original catalogs and adjust each stellar/Eris flux measurement by the value of the star flat at its detector location, and then repeat the entire calibration process. As a final quality-control step, we reject any measurement of Eris for which the χ^2 per degree of freedom (DOF) for the individual exposures' magnitudes within a time segment is >2.5. We drop the tilde and refer to these results as *V* magnitudes henceforth. The final catalog (included in Table 1) contains 45 measurements of Eris arising from ≈450 exposures on 42 distinct nights spanning 172 days, with a median uncertainty of 9 mmag. Figure 3 plots the results versus time.

2.3. Hubble Space Telescope

Each HST visit was composed of four 348 s exposures and one 585 s exposure in a single orbit. Six visits were initially planned to occur within one Dysnomia orbital period, based on the 15.774 day period reported by Brown & Schaller (2007). However, visit 3 (2018 January 3) suffered a tracking failure, so only two 348 s exposures were usable. An additional visit was awarded on 2018 February 3, at approximately the same orbital phase as visit 3, to offset these losses. The WFC3

Instrument Handbook[42] reports that the PSF FWHM is ∼67 mas at 0.60 μm, resulting in just over 7 pixels between Eris and Dysnomia at maximum elongation. Additional details on these HST observations can be found in Holler et al. (2021).

These images were retrieved from the Mikulski Archive for Space Telescopes (MAST) at the Space Telescope Science Institute (STScI). The raw images were reduced using the WFC3 pipeline, `calwf3 v.3.6.2` (released 2021 May 27),[43] which created a bad-pixel mask, corrected for bias, removed overscan regions, subtracted dark current, flat fielded, and normalized the fluxes between the separate UVIS1 and UVIS2 detectors. We make measurements on the `*flc.*` files that have had charge transfer efficiency (CTE) corrections applied.

We fit each UVIS2 image to a model in which the signal s_i in pixel i at location (x_i, y_i) is given by

$$s_i = b + f_{\mathrm{Dys}} P(x_i - x_0 - \Delta x, \, y_i - y_0 - \Delta y, \, g)$$
$$+ f_{\mathrm{Eris}} [P(x_i - x_0, \, y_i - y_0, \, g) \otimes D(R_{\mathrm{Eris}})]. \quad (4)$$

Here $P(x, y, g)$ is a PSF model for UVIS2 taken from tables created by Bellini et al. (2018).[44] We take the models for the *F606W* filter and interpolate them to the detector position of Eris's image. Bellini et al. (2018) found that the PSFs occupy a one-dimensional family of shapes; they tabulate PSFs for nine positions along this manifold. We assign a free parameter g to the group number that applies to any particular exposure, allowing it to be a floating point value from 0–8, with the PSFs linearly interpolated between their groups. For Eris, we convolve the PSF with a circular disk of finite angular radius R_{Eris}, with the brightness profile of a fully illuminated Lambertian hemisphere: $D \propto \sqrt{1 - (r/R_{\mathrm{Eris}})^2}$. The known radius (Sicardy et al. 2011) and distance of Eris imply a true angular diameter of 16.7 mas, or 0.42 WFC3 pixels, but we leave R_{Eris} as a free parameter since we do not know the surface brightness distribution of Eris. This could also be viewed as a generic adjustment of the PSF size to match the data. The background flux b, the fluxes f_{Dys} and f_{Eris}, and the center in pixel coordinates (x_0, y_0), of Eris are free parameters. The

---

[42] https://hst-docs.stsci.edu/wfc3ihb
[43] https://www.stsci.edu/files/live/sites/www/files/home/hst/instrumentation/wfc3/_documents/wfc3_dhb.pdf
[44] Because HST was tracking Eris at a nonsidereal rate, it would have been inaccurate to use stars in the exposures as PSF models, even if there were enough to form a high-S/N PSF model.
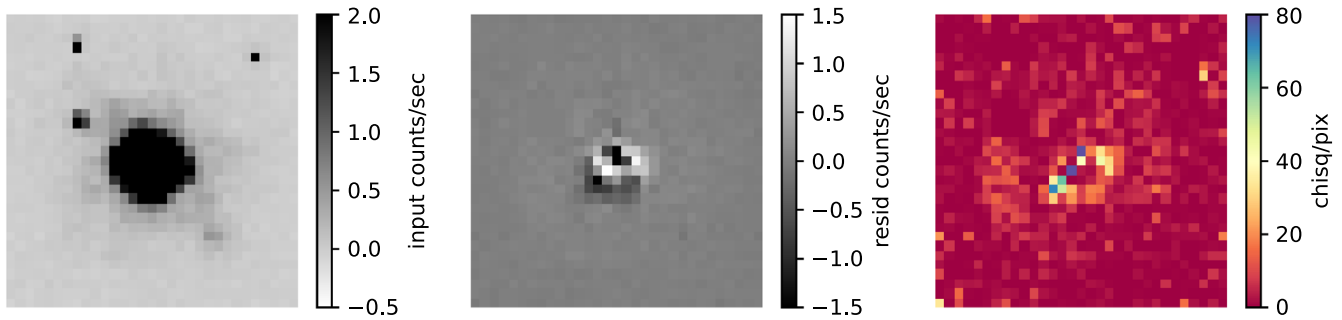
Figure 4. The model-fitting process for the HST exposures is shown for a random exposure, `idl004icq`. At left is the processed image from MAST, with CTE correction applied. At center are the residuals to a model of a PSF for Dysnomia (to the lower right of Eris in this image) and a disk-broadened PSF for Eris. At right, the residuals are re-plotted as the χ^2 per pixel using the pixel uncertainties reported by MAST. The residuals in the core of Eris are substantially larger than the statistical errors in the signal, due to the limitations of the PSF models. The residual fluxes can be compared to Eris's total flux of ≈ 800 counts s^{-1}.

displacement $(\Delta x, \Delta y)$ from Eris's center to Dysnomia is taken from the orbit derived by Holler et al. (2021). We minimize the χ^2 of the image data against the model with the free parameter set $\{f_{Eris}, f_{Dys}, b, x_0, y_0, g, R_{Eris}\}$. The model is linear in the first three parameters, and we report uncertainties on the fluxes from these linear fits. Pixels affected by cosmic rays are excluded from the fits.

As shown in Figure 4, the residuals to the model fits are well in excess of shot noise near the center of Eris, because the PSF models are not sufficiently accurate. To reduce the errors in the derived flux that arises from PSF inaccuracies, we sum the residuals to the fit in the central 9×9 pixels of Eris's image and add them back into the model-fitting flux. In essence, we are using a simple aperture flux within this region and then using PSF fitting to infer the remainder of Eris's flux. The 32 resulting magnitudes for Eris are listed in Table 1, along with their formal errors.

We expect the formal errors on Eris's flux (2.2 mmag for each of the shorter exposures) to be underestimates of the true uncertainty and derive an estimate of the additional systematic error in Section 3.3.

The χ^2 minimizations yield $R_{Eris} \approx 0.70$ pix, significantly larger than the known physical value. As noted above, this could be some combination of an inaccurate model for the disk's radial profile, or due to the PSF models being slightly too narrow, so we cannot draw any definitive conclusions about the nature of Eris's brightness distribution for this analysis.

The measurements of Dysnomia's magnitude have uncertainties of ~ 0.05 mag for the shorter exposures. We find that in order for the exposures within each orbit to be mutually consistent with a magnitude that remains constant over the ~ 45 minute duration of an orbit, we must add ~ 0.04 mag of systematic error allowance in quadrature to the magnitude uncertainty derived for each exposure. Once this is done, and the exposures within each orbit are averaged to a single value, we have seven measurements of Dysnomia's light curve, with typical accuracy of 0.025 mag. These are presented in Table 2.

2.4. Gaia

Following Szakáts et al. (2023), we extract observations of Eris from the Gaia DR3 (Gaia Collaboration et al. 2022; Tanga et al. 2022) table `gaiadr3_sso_observations`. There are 48 distinct observations spanning 2014–2017. In order to maintain independence from the Szakáts et al. (2023) result, we do not use the Gaia data in fitting periods or initial light curves,

but we do test whether the Gaia data are consistent with the light curve derived from the data sets discussed above. We do not attempt to assign a systematic error to Gaia's magnitudes. These data are included in Table 1.

3. Extraction of Period and Light Curve for Eris

3.1. Method

Given a set of measured magnitudes m_i with uncertainties σ_i taken at times t_i in filter bands b_i, we search for periodicity at frequency f by first adjusting the observation times for light-travel time and standardizing magnitudes to a (fictive) situation where the heliocentric and geocentric distances r and Δ to Eris were at a reference distance of $d_0 = 90$ au:

$$t_i \rightarrow t_i - \Delta_i/c \tag{5}$$

$$m_i \rightarrow m_i - 5\log_{10}(r_i \Delta_i / d_0^2). \tag{6}$$

We then fit the data to a model of sinusoidal variations including N_h harmonics, and a linear dependence of magnitude on Eris's solar phase angle ϕ_i (measured in degrees) at each epoch:

$$\hat{m}_i = m_{0,b_i} + \sum_{h=0}^{N_h} [A_h \cos 2\pi f t_i + B_h \sin 2\pi f t_i] + G\phi_i. \tag{7}$$

This model is linear in the parameters $\{m_{0,b}\}$ for the mean magnitudes per band, the amplitudes $\{A_h, B_h\}$ per harmonic, and the phase slope G. We scan across the nonlinear parameter f to produce a periodogram of $\chi^2 = \sum_i (m_i - \hat{m}_i)^2 / \sigma_i^2$ versus frequency. Note that we assume that the light curve and phase slopes are the same in all of the bands. This is more likely to be true for the g, r, G, $F606W$, and V bands, which are close to each other in central wavelength, than for the redder i and z bands. We examine the latter two bands after combining the former 5.

3.2. Estimating the Period

Because the P60 data are the only set that both resolved Eris's rotation period and spanned at least several cycles, we present their results in isolation first to identify plausible rotation periods. Fitting a simple sinusoid ($N_h = 0$) yields the periodogram shown atop Figure 5. We display only periods of $0 < f < 0.5$ cycles day^{-1} because the data were taken at nearly the same sidereal time each evening (as were the DES data); hence, signals at any other frequency would be strongly aliased
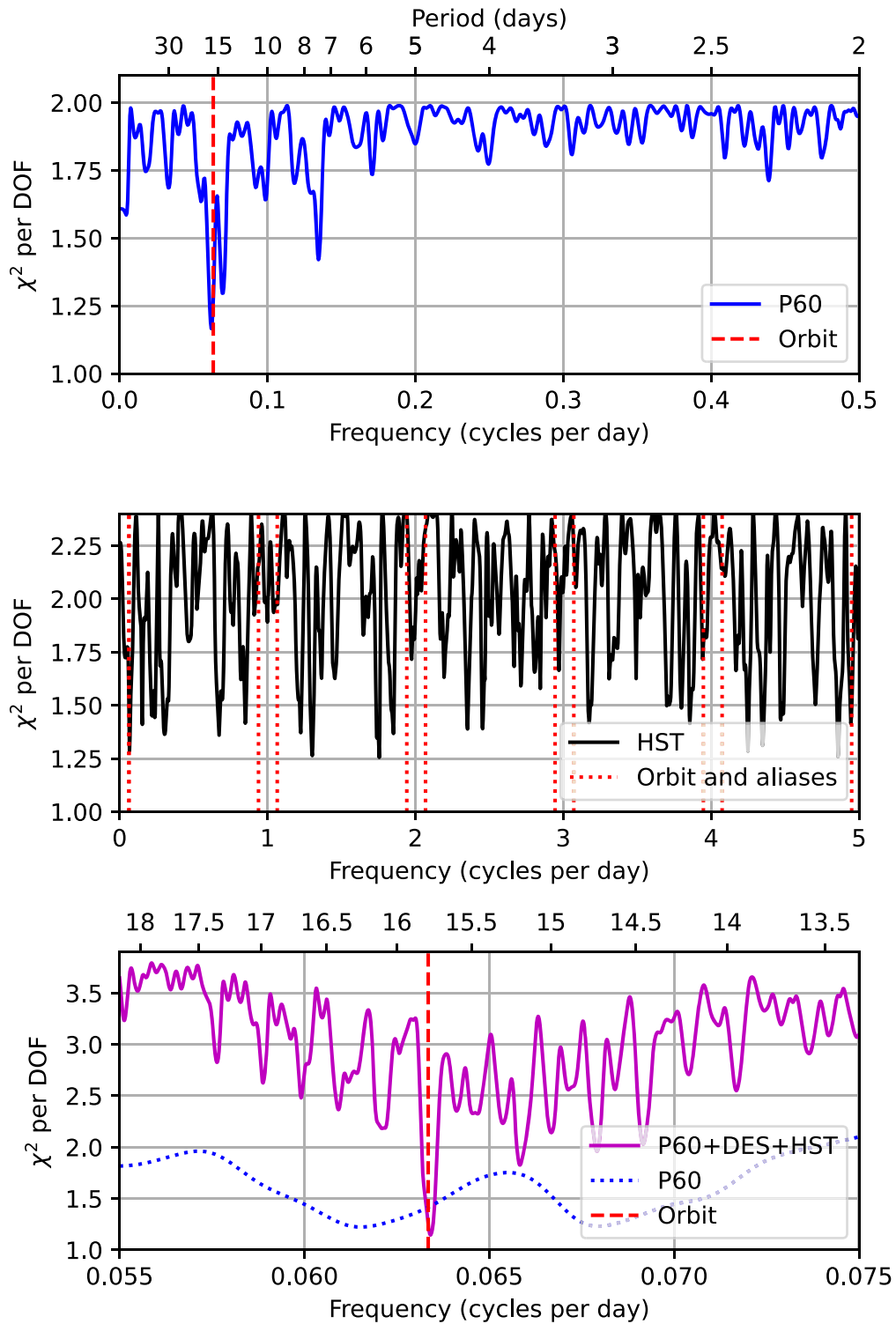
Figure 5. Each panel shows the χ^2 per DOF of a fit of a sinusoidal light curve to the photometric data vs. frequency. Ticks above the plots give period in days. The upper panel uses the only the P60 data, revealing two strong minima, at periods of 16.1 and 14.4 days. The former is consistent with the orbital period of Dysnomia, ~15.79 days, marked with the vertical dashed line. Aliases of these frequencies due to the sampling of once per sidereal day are also good fits; we plot only the range below the Nyquist frequency. The middle panel shows the χ^2/ DOF periodogram for the HST data, which are not subject to sidereal-day aliasing. The vertical lines mark the frequencies of synchronous rotation and all of its potential sidereal-day aliases with $P > 5$ hr. We can see that none of the possible $f > 0.5$/day aliases of the frequencies identified by the P60 data are good fits to a sinusoidal HST light curve. The lower panel shows the periodogram from joint consideration of the P60, HST, and DES g- and r-band data, after estimated systematic errors are applied to each and the light curve is allowed to have a harmonic. The data strongly select a photometric period consistent with Dysnomia's orbital frequency.

into this range. Two strong minima corresponding to periods of 16.1 and 14.4 days are apparent. Including a harmonic, $N_h = 1$, the same two peaks dominate, though additional minima appear

(as expected) at half of the original two frequencies, and their aliases. The first period is fully consistent with synchronous rotation at the orbital period of Dysnomia. The best-fit values

of the phase slope G are in the range of 0.07 mag degree^{-1}, which is plausible.

The HST data alone cover too short a time span to give a precise period, but they do offer multiple measurements at high S/N within roughly two cycles of the fundamental periods identified by the P60 data, and are not confined to fixed sidereal-time intervals. We use these in isolation to see if any of the aliases at $f > 0.5$ cycles day^{-1} are better fits than the $\sim$15 day periods identified by the P60 data. As shown in the middle panel of Figure 5, none of the aliases are consistent with the data, and we confine our further attention to the periods near 15 days indicated by the P60 light curve.

3.3. Fitting Combined Data

The P60+HST+DES data span $T \approx 5$ yr. If high-S/N data are available at either end of the time span, a shift in frequency of $\Delta f \approx 0.1/T$ will move the extremal points by 0.1 cycle on a phased light curve. A shift of this size away from the true f should therefore push at least one measurement to be a bad fit to the mean light curve. We therefore expect the uncertainty in the derived period, ΔP, to be roughly $\Delta P \approx \Delta f/f^2 = 0.1P^2/T \approx 0.02$ days. To summarize, the data being fit include:

1. 45 distinct observing segments in the V band from P60. We add in quadrature to each point's uncertainty an allowance of 12 mmag for systematic errors in photometry and calibration. This value is chosen to bring the χ^2 per DOF near unity for the best-fitting light curves.
2. $8 + 5$ observations in g and r, respectively, from DES. Each has 3 mmag of calibration systematic errors added in quadrature to its model-fitting error estimate, based on the comparison of DES stellar photometry to Gaia.
3. One mean magnitude for each of the seven orbits of HST data. Since the period is known to be much longer than the duration of a single HST orbit, we work with the per-orbit weighted-average magnitudes, which are listed in Table 2. We assign an independent systematic error of 3 mmag to each exposure before averaging; this is the value required to reduce the χ^2 per DOF to near unity for a model in which the magnitude was constant during each orbit.

The model of Equation (7) is then fit to these 65 measurements. Allowing for a single harmonic ($N_h = 1$), there are four free parameters for the periodic terms; four free mean magnitudes in g, r, V, and $F606W$; and one each for f and G. The lower panel of Figure 5 shows the resultant periodogram, which now strongly prefers a period consistent with the system's orbital period. If we formally estimate a 1σ confidence level as the range over which the χ^2 value increases by unity over its minimum, we obtain $P = 15.771 \pm 0.008$ days. The precision is in the range expected given the duration of the monitoring, and this $\pm 2\sigma$ confidence region includes the orbital period of $15.785\,899 \pm 0.000050$ days (Holler et al. 2021). The formal estimate of the uncertainty on the period is probably optimistic, given that we make some fairly crude allowances for systematic errors in the photometry, and assume a simple model for the light curve. In any case, we have strong evidence, independent of Szakáts et al. (2023), that the rotation period of Eris is within 1 part in 1000 of Dysnomia's orbital period. Henceforth, we will assume that Eris's rotation period is synchronous with Dysnomia's orbital period.

Note that the period measured from the light curve as viewed from Earth is essentially the synodic rotation period, whereas the reported Dysnomia orbital period is sidereal. The difference is, however, within the measurement uncertainties of the light-curve period: Eris is currently moving across the heliocentric sky at 0°.28 per year, leading to an apparent frequency shift of $\Delta f = (0°.28/360°)/\mathrm{yr} = 2 \times 10^{-6}/\mathrm{day}$. The apparent period difference should then be $\Delta P = P^2 \Delta f = 0.000\,5$ day, small enough to be ignored in our photometric analysis. We will also ignore any perturbation to the derived photometric period that might arise from precession of Eris's spin axis during the interval of our observations.

The top panel of Figure 6 shows the light curve, folded at the orbital period after removal of the mean magnitude and illumination-phase correction. The best-fit light curve has a center-to-peak amplitude of 0.015 mag at the fundamental and only 0.002 mag in the harmonic. Adding the harmonic does not induce a significant decrease in χ^2; hence, the light curve is very close to a single-peaked sinusoid. The best-fitting phase slope is $G = 0.05 \pm 0.01$ mag deg^{-1}, (Table 3) indicating a stronger opposition brightening than the slope of $G \approx 0.035$ mag degree^{-1} measured for Pluto by Buie et al. (2010), but weaker than the slope of ≈ 0.3 mag degree^{-1} they observed for Charon at phase angles of 0°.3–0°.5. Previous measures of the phase slope are summarized in Table 3 of Verbiscer et al. (2022). Our value is consistent with all of these lower-precision measures except perhaps the 0.105 ± 0.020 mag deg^{-1} measured in V band by Rabinowitz et al. (2007). The same authors report $G = -0.004 \pm 0.028$ mag deg^{-1} in the B band, and we are not able to reliably measure in our data such potential strong wavelength dependence.

The upper panel of Figure 6 also includes the G-band Gaia fluxes (magenta stars), averaged into eight phase bins. These agree perfectly in phase and amplitude with the light curve derived from the three other data sets, confirming the accuracy of the synchronous solution.

We remind the reader that the non-HST observations blend the flux of Dysnomia with that of Eris. But near the V band, Dysnomia's total light is only a ≈ 2 mmag perturbation to Eris's magnitude, so is an insignificant contributor to the light curve at current accuracy.

The DES i and z measurements are not well fit by a light curve with any sensible number of harmonics. The dashed curve in the central panel of Figure 6 shows the phased data and the best-fit $N_h = 1$ light curve. Indeed in each of these bands there are discrepant measurements at the same phase, suggesting measurement errors. There may be an unknown source of systematic errors in these bands. It is possible, for example, that Dysnomia's redder surface means that it is bright enough in iz to confound the PSF-fitting results on Eris's flux in a seeing-dependent way. We choose to ignore the iz data since any inference from it would be questionable.

The lower panel of Figure 6 shows the HST magnitudes for Dysnomia, averaged into HST orbits and phased at the orbital period. Similar to the HST Eris measurements, we determine the level of additional systematic error needed to make Dysnomia's fluxes within each orbit statistically consistent. This turns out to be about 0.04 mag, which we add in quadrature with the individual exposures' magnitude estimates before averaging by orbit. With only seven measurements over 30 days, it is impossible to determine a photometric period. The a priori expectation is, however, that if Eris were in
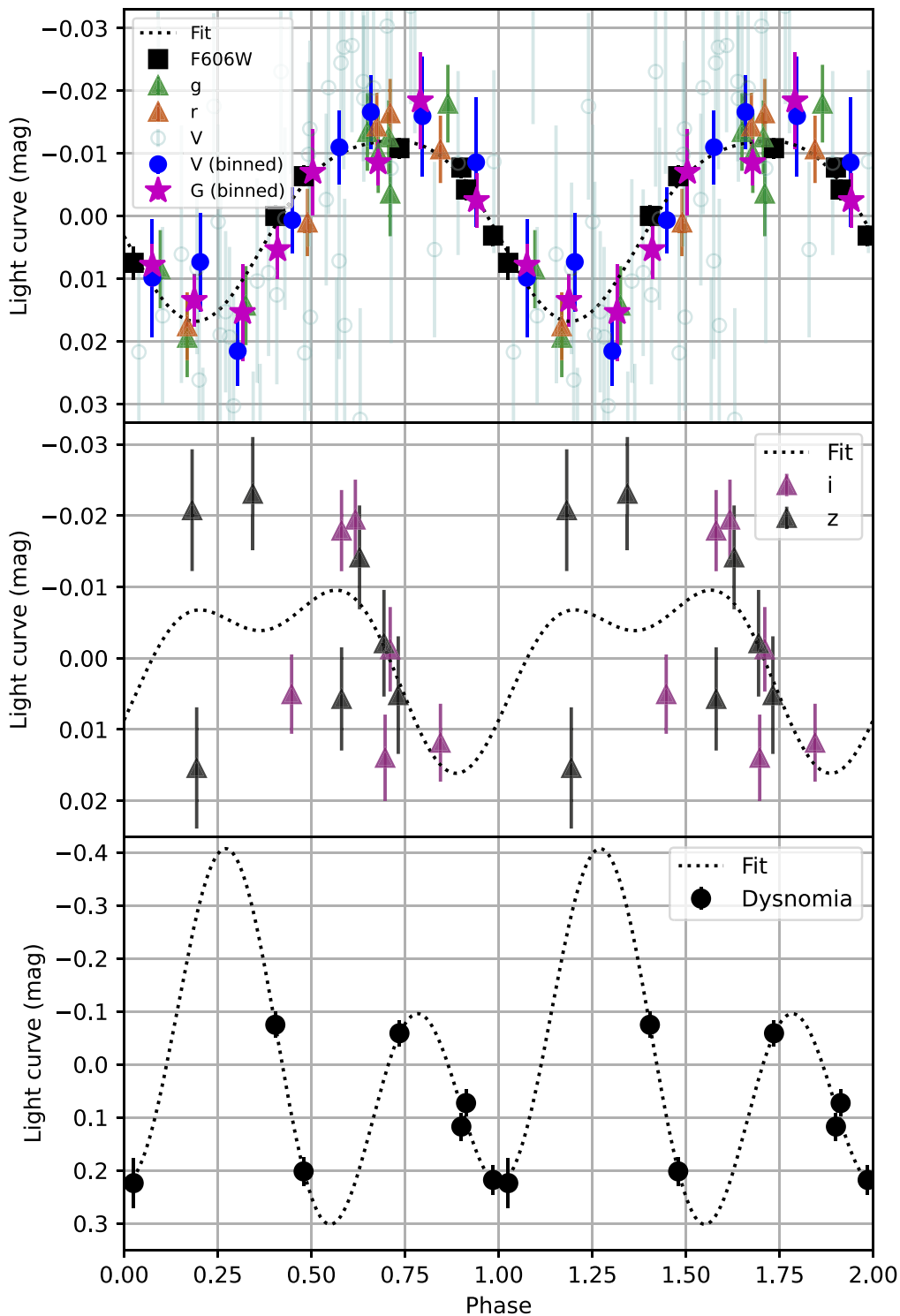
Figure 6. All panels show light curves folded at the orbital period of Dysnomia. Mean magnitudes and illumination-phase variation have been subtracted. The top panel shows the DES *g* and *r* bands (triangles), HST *F606W* data (squares), and the individual P60 *V*-band data (light cyan circles). The dashed line is the best-fit two-harmonic light curve, with 0.03 mag peak-to-peak amplitude. The blue circles are the P60 data binned into eight phase ranges. The magenta stars are the phase-binned Gaia *G*-band measures, which were *not* used to derive this light-curve fit. The central panel shows the DES *i* and *z* bands—the dotted curve is the best-fit light curve, and the data are clearly not consistent with even this best periodic model; we suspect there are uncorrected systematic errors in the *iz* photometry. The lower panel shows the HST magnitudes for Dysnomia. There is a clear variation of 0.3 mag, and they are plausibly fit by a double-peaked light curve from a fundamental and first-harmonic sinusoid, although there are only seven points, so this is certainly not conclusive.

synchronous rotation, then the less-massive Dysnomia would be as well. There is a clear detection of (at least) 0.3 mag peak-to-peak variability in Dysnomia's flux, and the light curve clearly is not sinusoidal at the orbital frequency. The dashed line in this panel is a fit to the simplest double-peaked light curve (a fundamental plus first-harmonic sinusoid). This shows

Table 3
Fitted Light-curve Parameters

Model	Period (days)	χ^2/DOF	G (mag deg^{-1})	A (mag)	θ_0 (deg)	C_2 (mag)	S_2 (mag)
With harmonic	15.771 ± 0.008	68.4/56	0.054 ± 0.012	0.015 ± 0.001	69 ± 5	$+0.003 \pm 0.001$	-0.001 ± 0.001
Fundamental only	15.771 ± 0.008	75.4/58	0.054 ± 0.012	0.013 ± 0.001	68 ± 4	$\equiv 0$	$\equiv 0$
Fundamental w/Gaia	15.769 ± 0.007	131.4/105	0.051 ± 0.011	0.013 ± 0.001	70 ± 4	$\equiv 0$	$\equiv 0$

Note. Values and uncertainties of the parameters of a fit to the combined data of the form in Equation (8), with and without allowing for a second harmonic. The first two lines omit Gaia data (thus matching the light curve shown in Figure 6) and are independent of Szakáts et al. (2023); the third line adds Gaia to the fit to give more total constraining power. The uncertainties are given as the values that result in an increase of $\Delta\chi^2 = 1$ from the best-fit value, after normalizing such that χ^2/DOF = 1 at the best fit. The uncertainties given are marginalized over all other free parameters. For parameters other than P, the values and uncertainties are given with the period fixed to Dysnomia's orbital period.

that a double-peaked light curve with a period equal to Dysnomia's orbital period is a plausible (though by no means unique) fit to the Dysnomia HST data.

Table 3 gives the quantitative results of fitting models with one or two sinusoidal components to the light curve with all data. Here it is apparent that the detection of the second harmonic is weak ($\Delta\chi^2 \approx -7$ for two additional DOFs). The quantities of potential physical interest—period, light-curve amplitude, and phase relation slope—are robust to the inclusion of the harmonic. Because the assigned systematic errors on our photometry, and the light-curve model, are approximations, the resulting uncertainties on fitted parameters may not represent an exactly 68% confidence region. The last row of Table 3 shows the fitted parameters when the Gaia data are included in the fit. All of the parameters shift by less than their estimated 1σ uncertainties. For the purposes of this table, we change the parameterization from Equation (7) to a form that isolates the total light-curve semiamplitude, A:

$$\hat{m}_i = m_{0,b_i} + G\phi_i + A\cos(\theta_i) + C_2\cos(2\theta_i) + S_2\sin(2\theta_i)$$

$$\theta_i = \frac{t_i - t_0}{P} \times 360° - \theta_0.$$

(8)

The time t_i is the time of emission of the light from Eris, and t_0 is the reference time JD 2457000. The parameter A gives the sinusoidal semiamplitude of the fundamental, and θ_0 is the phase relative to t_0 at which the fundamental reaches its minimum. C_2 and S_2 specify the harmonic signal, if included in the model.

4. Discussion

4.1. Origin of the Eris–Dynomia System

The initial orbital and physical conditions of the Eris–Dysnomia system are dependent on the formation mechanism. For example, a giant impact should create a Dysnomia interior to its current orbit, with subsequent evolution outward through the effects of tides. Conversely, if Dysnomia was captured, it is more likely that it started at a more distant semimajor axis and migrated inwards. If at any point Dysnomia's orbital period is shorter than (or retrograde to) Eris's rotation period, the tides raised on Eris by Dysnomia lag behind Dysnomia's position in its orbit, exerting a torque that transfers energy from Dysnomia's orbit to Eris and decreasing both Eris's rotation period and Dysnomia's semimajor axis. A more likely scenario is the opposite case, where Dysnomia's orbital period is longer than Eris's rotation period, transferring energy instead from

Eris to Dysnomia, which increases both Eris's rotation period and Dysnomia's orbital period. We quantify each of these scenarios using simplified equations for tidal evolution given by Goldreich & Peale (1968):

$$\dot{\omega}_E = \text{sign}(\Omega - \omega_E)\frac{15}{4}\frac{k_E}{Q_E}\frac{m_D}{m_E}\left(\frac{R_E}{a}\right)^3\frac{Gm_D}{a^3}$$ (9)

$$\dot{\omega}_D = \text{sign}(\Omega - \omega_D)\frac{15}{4}\frac{k_D}{Q_D}\frac{m_E}{m_D}\left(\frac{R_D}{a}\right)^3\frac{Gm_E}{a^3}.$$ (10)

In the above equations, $\dot{\omega}_E$ and $\dot{\omega}_D$ are the change in the rotational spin frequencies of Eris and Dysnomia, respectively; Ω is the mean motion of Dysnomia ($2\pi/P$); k_E and k_D are the respective tidal Love numbers for Eris and Dysnomia; Q_E and Q_D are their tidal quality factors; m_E and m_D are their masses; R_E and R_D are their radii; and a is the semimajor axis of Dysnomia's orbit.[45] A critical parameter will be the mass ratio $q = m_D/m_E$ of the system. The system mass ($M_{\text{tot}} = m_D + m_E = 1.6466 \times 10^{22}$ kg), system density (2.43 g cm^{-3}), and current semimajor axis ($a_o = 37,273$ km) were all taken from Holler et al. (2021). The Eris radius ($R_E = 1163$ km) was taken from Sicardy et al. (2011). Other parameters are less precisely known. Brown & Butler (2018) estimated a Dysnomia radius $R_D = 350 \pm 57.5$ km from their weak millimeter-wave detection of Dysnomia. Nominal values for the tidal quality factor were taken as $Q_E = Q_D = 100$, and the tidal Love numbers for Eris and Dysnomia were calculated as described in Murray & Dermott (2000), with the rigidity of an icy body, μ, taken to be 4×10^9 Nm^{-2} (Hastings et al. 2016). A nominal density for Dysnomia was assumed to be 1.2 g cm^{-3}, less than half of the system density. In this case, the nominal radius from Brown & Butler (2018) yields a mass ratio $q = 0.014$.

These equations can be coupled with the conservation of the system's angular momentum to solve for the time evolution of the system given the (unknown) initial and (known) final states. This can be done numerically, following Hastings et al. (2016), as elaborated for the Eris–Dysnomia system in Szakáts et al. (2023). An analytic solution is available as well

---

[45] The tidal Love number, k, is a dimensionless parameter that defines the rigidity of a body, i.e., how strongly the body will deform due to tidal forces. The tidal quality factor, Q, is a dimensionless measure of the deformation of an object divided by the energy dissipated via heat due to the deformation; high Q values indicate a less efficient dissipation of energy due to tidal stresses. The ratio of the tidal Love number to the tidal quality factor gives the dimensionless rate of the internal energy dissipation for the body being considered, with smaller numbers indicating lower dissipation and slower orbital migration.
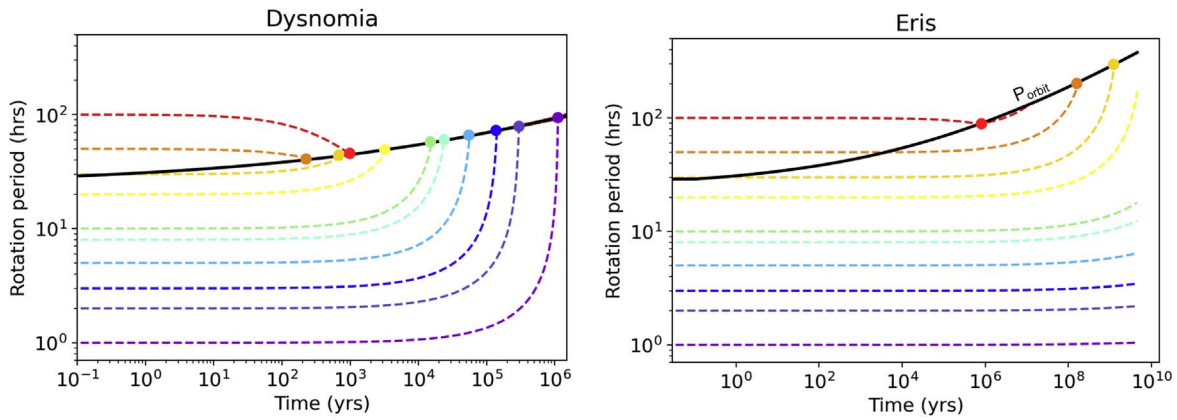
Figure 7. Numerically integrated examples of potential evolution of Dysnomia's (left) and Eris's (right) rotation periods, based on the method described in Hastings et al. (2016). All examples assume an initial orbit at $3 \times$ the Roche radius, with a Dysnomia density of $1.2 \, \text{g cm}^{-3}$ and nominal k and Q values. Different initial rotation periods are represented by colored dashed lines and correspond to 1, 2, 3, 5, 8, 10, 20, 30, 50, and 100 hr. The black solid curve represents the orbital period as a function of time in each plot. When a rotation period reaches the orbital period, it becomes locked, as indicated by the colored-circle endpoints. When both bodies synchronize, the orbital evolution halts. At this Dysnomia density, Dysnomia's rotation and orbital periods synchronize in ∼1 Myr, and Eris's rotation synchronizes within 4.5 Gyr for minimum initial periods ≳20 hr.

(e.g., Murray & Dermott 2000), as we recapitulate in the Appendix, and yields the expected time interval $t_0 - t_b$ between the birth of the system and the attainment of synchronous Eris rotation as

$$t_0 - t_b \approx q^{-1} P_0 \left(\frac{a_0}{R_E} \right)^5 \frac{1}{39\pi} \frac{Q_E}{k_E} \left| 1 - \left(\frac{a_b}{a_0} \right)^{13/2} \right| \qquad (11)$$

$$= (12.5 \, \text{Myr}) \times q^{-1} \left(\frac{Q_E}{100} \right) \left(\frac{0.1}{k_E} \right) \left| 1 - \left(\frac{a_b}{a_0} \right)^{13/2} \right|. \qquad (12)$$

4.1.1. Outward Migration

To illustrate the nature of outward migration, Figure 7 plots the history of Ω, ω_D, and ω_E in numerical integrations of scenarios in which Dysnomia is formed well interior to its current orbit, at an initial semimajor axis of $a_b = 6000$ km, ∼3× the nominal Roche limit. We consider a range of initial rotation periods from 1–100 hr for Eris. Note that only one of these initial rotation periods would match the current total angular momentum of the system; these graphs show illustrative behavior, not models of the system.

The integrations indicate that Dysnomia's rotation and orbital periods synchronize in ∼1 Myr. This value varies less than an order of magnitude when considering Dysnomia densities ranging from 0.8–2.43 g cm^{-3}. The minimum initial Eris rotation period that results in synchronization within 4.5 Gyr is highly dependent on the assumed density of Dysnomia. This plot assumes a density of 1.2 g cm^{-3} for Dysnomia, and it is seen that the initial rotation period of Eris must be ≳20 hr to reach synchronization, whereas the average satellite-free TNO has a period of roughly 10 hr (Lacerda & Luu 2006; Thirouin et al. 2014). Note that at the chosen values of ρ_D and a_b, an initial orbital period near 20 hr is required if we wish to both obtain the current synchronous period and do so within 4.5 Gyr. But the initial period that synchronizes in 4.5 Gyr varies from 2–30 hr as Dysnomia's density varies from 2.43 g cm^{-3} to 0.8 g cm^{-3}. Thus synchronization is attainable for at least part of the space of plausible initial conditions with near-Roche orbits. In the

high-density Dysnomia case, the minimum initial period that results in synchronous rotation is shorter than Eris's critical rotation period[46] of 2.12 hr, assuming Eris's density is comparable to the system density, and hence implausible.

The analytic solution in Equation (12) clarifies the constraints on the system. If we require that synchronous rotation of Eris be attained in less than 4.6 Gyr, and that the system have the current total angular momentum, the minimum mass ratio of Dysnomia to Eris is

$$q > 0.003 \left(\frac{Q_E}{100} \right) \left(\frac{0.1}{k_E} \right). \qquad (13)$$

This bound is easily satisfied at the nominal Q_E and k_E, since the measured 350 km radius of Dysnomia implies a volume ratio of 0.027. Thus, Eris is easily brought into synchronous rotation in scenarios in which Dysnomia forms well interior to the current orbit, even with Q as high as 1000 for Eris.

The hydrodynamic modeling performed to explain the formation of the Pluto–Charon system (Canup 2005), and the strong resemblance of Eris–Dysnomia to Pluto–Charon, have implications for the formation of the satellites of other large TNOs (Figure 1) and the possible presence of other satellites in the Eris–Dysnomia system. The prevalence of other large TNO binary systems similar to Pluto–Charon and Eris–Dysnomia (e.g., Orcus-Vanth, Salacia-Actaea, and Varda-Ilmarë) implies a dynamically chaotic past for the trans-Neptunian region and a possible selection effect for the binaries observed today. It is possible that the only systems that survived were those that underwent a grazing collision, as proposed for the formation of the Pluto–Charon system, while objects that were more thoroughly collisionally disrupted would not have survived. The latter could have resulted in numerous collisional families scattered throughout the trans-Neptunian region, similar to

---

[46] The *critical rotation period* is the rotation period that results in equivalent rotational and gravitational potential energies for a point mass on the surface of the body, and is defined as $P_{\text{crit}} = \sqrt{\frac{3\pi}{G\rho}}$. For $P < P_{\text{crit}}$, the rotational energy exceeds the gravitational potential energy and the body starts to break up. Note that this definition assumes a strengthless object; a real object with nonzero material strength would have a shorter critical rotation period, so this definition provides an upper limit to P_{crit}.

those among the main belt asteroids. Whether the density of the early Kuiper Belt region was sufficient to produce numerous large-body collisions is, however, questionable (Campo Bagatin et al. 2016).

The Pluto–Charon system is also home to four minor satellites in orbits beyond Charon (Weaver et al. 2006; Showalter et al. 2011, 2012) that likely formed from the debris disk of the Pluto–Charon forming giant impact (Canup 2011). A search for minor satellites of Eris using the same HST WFC3 data in this work was performed by Murray et al. (2018), with an imaging depth just capable of identifying satellites comparable to Nix and Hydra (the largest of Pluto's minor satellites at ≈50 km diameter) at the distance of Eris (∼96 au). No satellites were identified, meaning the formation of the Pluto–Charon system was the result of more unique circumstances, or any minor satellites around Eris are fainter than Nix and Hydra. Perhaps even more interesting is the claim that Eris may have an unresolved satellite interior to Dysnomia's orbit. This was proposed by Spencer et al. (2021) to explain the statistically significant non-Keplerian nature of Dysnomia's orbit (Holler et al. 2021), but can now be highly constrained given the rotation period determined in this work and in Szakáts et al. (2023). If such a moon M exerted a tidal torque on Eris stronger than Dysnomia can currently exert, then the synchronization of Eris's rotation to Dysnomia would be broken. Equation (9) gives a torque $\propto m^2/a^6$ of the moon. Any moon that was not resolved from Eris by HST would be ≲0″.1 away from Eris, or at a semimajor axis $a_M \lesssim a_D/5$. We can estimate, therefore, that any close-in moon with mass $m_M > (a_M/a_D)^{-3}m_D = m_D/125$ would break the observed synchronous rotation of Eris. This also constrains the diameter of such an inner moon to <140 km if it has the same density as Dysnomia.

4.1.2. Inward Migration

The radically different albedos and colors of Eris and Dysnomia might suggest a scenario in which Dysnomia was captured into a retrograde orbit at semimajor axis $a_b > a_0$, and tidal migration was inwards. In this case, attainment of synchronous Eris rotation within 4.6 Gyr under Equation (12) implies

$$\frac{a_b}{a_0} < 1.42 \left[\left(\frac{q}{0.027}\right) \left(\frac{100}{Q_E}\right) \left(\frac{k_E}{0.1}\right) \right]^{2/13}. \qquad (14)$$

This a_b is roughly 1% of the Hill radius of Eris when it is at perihelion, 38 au from the Sun. We can also investigate the rotational period P_{Eb} that Eris would need to have at the time of capture. Ignoring the spin angular momentum of Dysnomia as unimportant, conservation of angular momentum requires

$$1 + \ell_p = -\ell_p \frac{P_0}{P_{Eb}} + \left(\frac{a_b}{a_0}\right)^{1/2}$$

$$\Rightarrow \frac{P_0}{P_{Eb}} = \ell_p^{-1} \left[\left(\frac{a_b}{a_0}\right)^{1/2} - 1 - \ell_p \right]$$

$$\lesssim \ell_p^{-1} \left[\left(\frac{0.027 \times 4.6 \text{ Gyr}}{12.5 \text{ Myr}}\right)^{1/13} - 1 \right]$$

$$\approx 300q \lesssim 10. \qquad (15)$$

In this evaluation, we have set to unity the intrinsic physical quantity ratios that are raised to the 1/13 power, and make use of the current ratio ℓ_p of Eris's spin angular momentum to the system orbital angular momentum (see the Appendix). A precapture Eris rotation period of $P_{Eb} \approx 10$ h, similar to the mean <10 hr periods reported for nonbinary TNOs by Lacerda & Luu (2006) and Thirouin et al. (2014), would have $P_0/P_{Eb} = 38$. According to Equation (15), such a large period change is only possible during the modest ≈40% decrease in orbital radius that is achievable in <4.6 Gyr if we have $q > 0.13$. A Dysnomia mass this large is not consistent with the reported size ratio of Dysnomia to Eris. The capture theory is difficult to reconcile with synchronous rotation of Eris unless some other event slowed Eris's rotation beforehand.

4.2. The Surface of Eris

The measured peak-to-valley amplitude from the Eris light curve is small at 3%, but nonzero. Stellar occultation timing on two chords from Sicardy et al. (2011) favors a spherical projected shape for Eris, but few-percent deviations from sphericity can probably not be excluded by these data. Nonetheless, a nonspherical ellipsoidal shape for Eris would lead to a double-peaked light curve, which would mean that our detected photometric period would correspond to rotation at precisely half the orbital period of Dysnomia. This seems highly unlikely given the nearly circular orbit of Dysnomia ($e < 0.01$; Holler et al. 2021), so it seems more likely that Eris's variability is dominated by longitudinal variations in albedo.

Albedo variations on Eris's surface are highly plausible given the large variation of surface albedos on Pluto (Buratti et al. 2017), and the high mean albedo of Eris ($p = 0.96^{+0.09}_{-0.04}$, Sicardy et al. 2011) suggests some form of frost generation, and seasonal nitrogen cycling is suggested by the models of Hofgartner et al. (2019).

Dysnomia's orbit is currently inclined by ≈45° to the line of sight, so if this orbit is close to equatorial, Eris's rotation pole is sufficiently inclined to bring a substantial fraction of its surface in and out of view during rotation. The surface variation in albedo must clearly exceed 3% to generate the light curve, but otherwise a wide range of dark-patch albedos, sizes, and geometries could be conjured to produce the observed light curve. The few-percent albedo difference between the regions of the surface that rotate into and out of view are small compared to the hemispherical differences observed on Pluto (e.g., Buratti et al. 2017), suggesting that Eris lacks large-scale features as contrastive as Pluto's Sputnik Planitia and Cthulhu Macula.

4.3. The Surface of Dysnomia

The double-peaked and high-amplitude Dysnomia light curve (lower panel of Figure 6) is what would be expected from a substantially asymmetric body in synchronous rotation, but Dysnomia's estimated diameter of 700 ± 115 km (Brown & Butler 2018) is large enough that significant deviations from a sphere are not expected. Instead, this could indicate large dichotomies in Dysnomia's surface composition, manifesting as large dichotomies in color and albedo. Unfortunately, the HST data used to construct the light curve were obtained only through the F606W filter, so no phase-dependent color information is available. Additionally, with the nonconclusive,

sparsely sampled light curve and no occultation data to back up the assumption that Dysnomia is spherical, its surface properties remain entirely unconstrained, and it could in fact be ellipsoidal in shape with a double-peaked light curve. As a relatively bright TNO satellite around the most-massive known TNO, Dysnomia is a prime target for the next level of study, which would include higher-cadence photometric observations and phase-resolved color and spectroscopic observations in order to understand the interactions between the two bodies and the ongoing evolution of the system.

5. Summary

We use three Earth-based data sets from the Palomar 60 inch telescope (high cadence), DES (long time baseline), and the Hubble Space Telescope (high photometric precision and nonsidereal sampling) to confirm the synchronous rotation of the TNO dwarf planet Eris first reported in Szakáts et al. (2023). Highlights of the results and interpretations include:

1. The rotation period of Eris is determined to be 15.771 ± 0.008 days, within 2σ of the orbital period of Dysnomia determined by Holler et al. (2021), $15.785\,899 \pm 0.000050$ days.
2. The amplitude of Eris's light curve is only 0.03 mag, suggesting that any large-scale albedo features such as Pluto's Sputnik Planitia and Cthulhu Macula that rotate in and out of the field of view have albedo variations of $\lesssim 10\%$. Smaller features with larger albedo variation are also plausible.
3. Eris's illumination-phase slope of 0.05 mag per degree is between Pluto's and Charon's, implying a surface texture intermediate between those two objects.
4. The light curve of Dysnomia from HST WFC3 data is consistent with a synchronous period as well, but the small number of data points prevents a definitive determination. The large light-curve amplitude of 0.3 mag ($10\times$ larger than Eris's amplitude) is consistent with an ellipsoidal object or a spherical object with large-scale surface dichotomies.
5. The formation of the Eris–Dysnomia system is best explained by a giant-impact origin, including reasonable estimates for the initial rotation period of Eris, the initial semimajor axis of Dysnomia, and the density of Dysnomia. Tidal evolution of Eris due to the inward migration of Dysnomia after capture from heliocentric orbit is difficult to accommodate within the age of the solar system.

Acknowledgments

Appendix
Analytic Solution for Tidal Locking Timescale

We summarize here an analytic solution to the most basic equations for the time to reach synchronous rotation of a satellite (s) and planet (p) to their orbit frequency $\Omega = 2\pi / P$. The result for the synchronization time in Equation (A9) agrees with that given, for example, by Equation (4.123) of Murray & Dermott (2000). We assume the two bodies have masses M_p and M_s such that $M_p + M_s = M_{\rm tot}$ and $q = M_s/M_p$. We assume a circular orbit at semimajor axis a such that $GM_{\rm tot} = \Omega^2 a^3$. If the radii are R_p and R_s, we also have the density relation $q = \rho_s R_s^3 / \rho_p R_p^3$. The sum of the planet's and satellite's spin angular momenta and the orbital angular momentum is conserved, giving us:

$$\frac{L_{\rm tot}}{M_p} = L_p + L_s + L_{\rm orb}(\Omega)$$
$$= L_p + L_s + \frac{q}{1+q} M_{\rm tot}(GM_{\rm tot})^{2/3}\Omega^{-1/3} \qquad (A1)$$

$$\Rightarrow \tau_p + \tau_s = \frac{M_{\rm tot}}{3}\frac{q}{1+q}(GM_{\rm tot})^{2/3}\Omega^{-4/3}\dot{\Omega}, \qquad (A2)$$

where τ_p is the torque on the planet due to tides raised on it by the satellite, and τ_s vice versa. Equation (6) of Goldreich & Peale (1968) approximates τ_p generated on the planet by the tides raised on it from the satellite's mass as

$$\tau_p = -\frac{3k_p}{2Q_p}\frac{GM_s^2 R_p^5}{a^6}s_p,$$
$$= -\frac{3M_{\rm tot}}{2}\frac{k_p}{Q_p}\frac{q^2}{(1+q)^2}R_p^5(GM_{\rm tot})^{-1}\Omega^4 s_p$$
$$s_p \equiv {\rm sign}(\omega_p - \Omega). \qquad (A3)$$

We introduce a dimensionless parameter giving the ratio of the torques (omitting the sign factors)

$$T \equiv \frac{\tau_s}{\tau_p} = \frac{k_s}{k_p}\frac{Q_p M_p^2 R_s^5}{Q_s M_s^2 R_p^5}$$
$$\approx \frac{\mu_p \rho_s g_s R_s}{\mu_s \rho_p g_p R_p}\frac{Q_p M_p^2 R_s^5}{Q_s M_s^2 R_p^5}$$
$$= \frac{\mu_p}{\mu_s}\frac{Q_p}{Q_s}\left(\frac{\rho_s}{\rho_p}\right)^{-1/3}q^{1/3}. \qquad (A4)$$

In the second line, we have taken the standard formula for the tidal Love number k (Equation (3) from Goldreich & Peale 1968) and approximated

$$k = \frac{3}{2\left(1 + \frac{19\mu}{2\rho g R}\right)} \approx \frac{3\rho g R}{19\mu}, \qquad (A5)$$

where μ and g are the rigidity and surface gravity of the body, respectively, and we have approximated that the μ term dominates the denominator. Note that T is entirely determined by the ratios of intrinsic physical characteristics of the planet and satellite, times $q^{1/3}$.

Combining Equations (A2), (A3), and (A4), we obtain a differential equation in Ω and its solution for the time interval between an initial state i and final state f as

$$\dot{\Omega} = \frac{-9k_p}{2Q_p}q(GM_{\rm tot})^{-5/3}R_p^5(s_p + Ts_s)\Omega^{16/3} \qquad (A6)$$

$$\Rightarrow \quad t_f - t_i = \tilde{t}\left[\left(\frac{\Omega_f}{\Omega_0}\right)^{-13/3} - \left(\frac{\Omega_i}{\Omega_0}\right)^{-13/3}\right](s_p + Ts_s)^{-1}$$
$$(A7)$$

$$= \tilde{t}\left[\left(\frac{a_f}{a_0}\right)^{13/2} - \left(\frac{a_i}{a_0}\right)^{13/2}\right](s_p + Ts_s)^{-1} \qquad (A8)$$

$$\tilde{t} \equiv \frac{2k_p}{39Q_p}q^{-1}R_p^5(GM_{\rm tot})^{5/3}\Omega_0^{-13/3}$$
$$= q^{-1}P_0\left(\frac{a_0}{R_p}\right)^5\frac{1}{39\pi}\frac{Q_p}{k_p}, \qquad (A9)$$

with P_0 and a_0 being period and semimajor axis of the orbit at a reference time, respectively, which we will make the present day for the Eris–Dysnomia system.

Equation (A8) applies for any interval over which s_p and s_s are constant. Consider a scenario for which the system is born at some time t_b into an orbit with radius $a_b < a_0$; then both planet and satellite spin down until a time t_s when the satellite synchronizes to the orbit; then the planet spins down until a time t_0 at which the system is doubly synchronous and attains the current orbital configuration. The time interval $t_b \to t_s$ has $s_p = s_s = 1$, and then switches to $s_p = 1$, $s_s = 0$ for

$t_s < t < t_0$. The total time to planet synchronization becomes

$$t_0 - t_b = (t_0 - t_s) + (t_s - t_b)$$

$$= \tilde{t} \left\{ 1 - \left(\frac{a_b}{a_0} \right)^{13/2} + \frac{T}{1+T} \left[\left(\frac{a_s}{a_0} \right)^{13/2} \right. \right.$$

$$\left. \left. - \left(\frac{a_b}{a_0} \right)^{13/2} \right] \right\}. \tag{A10}$$

The 13/2 power of a/a_0 appearing in these solutions implies that the time to establishing a doubly locked system is going to be $\tilde{t}$ to within a factor 2, unless the orbit has expanded $<10\%$ since satellite synchronization.

Should we wish to investigate in more detail and solve for the factor multiplying $\tilde{t}$, we can introduce two more dimensionless parameters: $f_s \equiv L_{sb}/L_{pb}$ is the ratio of the spin angular momenta at birth, and we expect $f_s \ll 1$ for a system with $q \approx 0.01$, like Eris–Dysnomia. The condition that the satellite synchronizes first is $f_s T < 1$. We also introduce $\ell_p \approx q^{-1}(a/R_p)^2$ as the ratio L_p/L_{orb} after synchronization. If we take L_s/L_{orb} to be negligible, then the angular momentum conservation between the three epochs t_b, t_s, and t_0 becomes

$$L_{pb}(1 + f_s) + L_{\mathrm{orb}}(a_b) = L_{pb}(1 - f_s T)$$
$$+ L_{\mathrm{orb}}(a_s) = (1 + \ell_p) L_{\mathrm{orb}}(a_0), \tag{A11}$$

which, using $L_{\mathrm{orb}} \propto \sqrt{a}$, can be solved to yield

$$\left(\frac{a_s}{a_0} \right)^{13/2} = (1 + f_s)^{-13} \left[(1 + \ell_p) f_s \frac{1 - T}{1 + T} \right.$$

$$\left. + (1 - f_s T) \sqrt{\frac{a_b}{a_0}} \right]^{13}. \tag{A12}$$

As long as $f_s < 1$ and $a_b < 0.8$ or so, the bracketed quantity in Equation (A10) will be close to unity, and the synchronization time will be $\tilde{t}$.

ORCID iDs

Gary M. Bernstein https://orcid.org/0000-0002-8613-8259
Bryan J. Holler https://orcid.org/0000-0002-6117-0164
Rosario Navarro-Escamilla https://orcid.org/0009-0009-2907-5421
Pedro H. Bernardinelli https://orcid.org/0000-0003-0743-9422
T. M. C. Abbott https://orcid.org/0000-0003-1587-3931
M. Aguena https://orcid.org/0000-0001-5679-6747
O. Alves https://orcid.org/0000-0002-7394-9466
J. Annis https://orcid.org/0000-0002-0609-3987
D. Bacon https://orcid.org/0000-0002-2562-8537
D. Brooks https://orcid.org/0000-0002-8458-5047
D. L. Burke https://orcid.org/0000-0003-1866-1950
A. Carnero Rosell https://orcid.org/0000-0003-3044-5150
J. Carretero https://orcid.org/0000-0002-3130-0204
L. N. da Costa https://orcid.org/0000-0002-7731-277X
M. E. S. Pereira https://orcid.org/0000-0002-7131-7684
J. De Vicente https://orcid.org/0000-0001-8318-6813
S. Desai https://orcid.org/0000-0002-0466-3288
A. Drlica-Wagner https://orcid.org/0000-0001-8251-933X
S. Everett https://orcid.org/0000-0002-3745-2882
I. Ferrero https://orcid.org/0000-0002-1295-1132
J. García-Bellido https://orcid.org/0000-0002-9370-8360
D. W. Gerdes https://orcid.org/0000-0001-6942-2736
D. Gruen https://orcid.org/0000-0003-3270-7644
S. R. Hinton https://orcid.org/0000-0003-2071-9349
D. L. Hollowood https://orcid.org/0000-0002-9369-4157
D. J. James https://orcid.org/0000-0001-5160-4486
K. Kuehn https://orcid.org/0000-0003-0120-0808
N. Kuropatkin https://orcid.org/0000-0003-2511-0946
J. Mena-Fernández https://orcid.org/0000-0001-9497-7266
R. Miquel https://orcid.org/0000-0002-6610-4836
R. L. C. Ogando https://orcid.org/0000-0003-2120-1154
A. Pieres https://orcid.org/0000-0001-9186-6042
A. A. Plazas Malagón https://orcid.org/0000-0002-2598-0514
E. Sanchez https://orcid.org/0000-0002-9646-8198
M. Smith https://orcid.org/0000-0002-3321-1432
M. Soares-Santos https://orcid.org/0000-0001-6082-8529
E. Suchyta https://orcid.org/0000-0002-7047-9358
M. E. C. Swanson https://orcid.org/0000-0002-1488-8552

References

Abbott, T. M. C., Adamów, M., Aguena, M., et al. 2021, ApJS, 255, 20
Adams, E. R., Gulbis, A. A. S., Elliot, J. L., et al. 2014, AJ, 148, 55
Astakhov, S. A., Lee, E. A., & Farrelly, D. 2005, MNRAS, 360, 401
Bannister, M. T., Gladman, B. J., Kavelaars, J. J., et al. 2018, ApJS, 236, 18
Bellini, A., Anderson, J., & Grogin, N. A. 2018, Focus-diverse, empirical PSF models for the ACS/WFC, Instrument Science Report ACS 2018-8
Benecchi, S. D., Noll, K. S., Grundy, W. M., et al. 2009, Icar, 200, 292
Bernardinelli, P. H., Bernstein, G. M., Jindal, N., et al. 2023, arXiv:2304.03017
Bernardinelli, P. H., Bernstein, G. M., Sako, M., et al. 2022, ApJS, 258, 41
Bernstein, G. M., Abbott, T. M. C., Armstrong, R., et al. 2018, PASP, 130, 054501
Bertin, E. 2011, in ASP Conf. Ser. 442, Astronomical Data Analysis Software and Systems XX, ed. I. N. Evans et al. (San Francisco, CA: ASP), 435
Bertin, E., & Arnouts, S. 1996, A&AS, 117, 393
Blagorodnova, N., Neill, J. D., Walters, R., et al. 2018, PASP, 130, 035003
Brown, M. E., & Butler, B. J. 2018, AJ, 156, 164
Brown, M. E., & Schaller, E. L. 2007, Sci, 316, 1585
Brown, M. E., van Dam, M. A., Bouchez, A. H., et al. 2006, ApJL, 639, L43
Brunini, A., & López, M. C. 2020, MNRAS, 499, 4206
Buie, M. W., Grundy, W. M., Young, E. F., Young, L. A., & Stern, S. A. 2010, AJ, 139, 1117
Buratti, B. J., Hofgartner, J. D., Hicks, M. D., et al. 2017, Icar, 287, 207
Burke, D. L., Rykoff, E. S., Allam, S., et al. 2018, AJ, 155, 41
Campo Bagatin, A., Benavidez, P. G., Ortiz, J. L., & Gil-Hutton, R. 2016, MNRAS, 461, 2060
Canup, R. M. 2005, Sci, 307, 546
Canup, R. M. 2011, AJ, 141, 35
Carraro, G., Maris, M., Bertin, D., & Parisi, M. G. 2006, A&A, 460, L39
Cenko, S. B., Fox, D. B., Moon, D.-S., et al. 2006, PASP, 118, 1396
Dones, L., Brasser, R., Kaib, N., & Rickman, H. 2015, SSRv, 197, 191
Duffard, R., Ortiz, J. L., Santos Sanz, P., et al. 2008, A&A, 479, 877
Elliot, J. L., Kern, S. D., Clancy, K. B., et al. 2005, AJ, 129, 1117
Fernandez, J. A., & Ip, W. H. 1984, Icar, 58, 109
Funato, Y., Makino, J., Hut, P., Kokubo, E., & Kinoshita, D. 2004, Natur, 427, 518
Gaia Collaboration, Vallenari, A., Brown, A. G. A., et al. 2022, arXiv:2208.00211
Gladman, B., Marsden, B. G., & Vanlaerhoven, C. 2008, in The Solar System Beyond Neptune, ed. M. A. Barucci et al. (Tucson, AZ: Univ. Arizona Press), 43
Goldreich, P., Lithwick, Y., & Sari, R. 2002, Natur, 420, 643
Goldreich, P., & Peale, S. J. 1968, ARA&A, 6, 287
Gomes, R., Levison, H. F., Tsiganis, K., & Morbidelli, A. 2005, Natur, 435, 466
Grundy, W. M., Noll, K. S., Nimmo, F., et al. 2011, Icar, 213, 678
Grundy, W. M., Noll, K. S., Roe, H. G., et al. 2019, Icar, 334, 62
Hahn, J. M., & Malhotra, R. 2005, AJ, 130, 2392
Hastings, D. M., Ragozzine, D., Fabrycky, D. C., et al. 2016, AJ, 152, 195
Hofgartner, J. D., Buratti, B. J., Hayne, P. O., & Young, L. A. 2019, Icar, 334, 52

Holler, B. J., Grundy, W. M., Buie, M. W., & Noll, K. S. 2021, Icar, 355, 114130

Johansen, A., Youdin, A., & Mac Low, M.-M. 2009, ApJL, 704, L75

Kominami, J. D., Makino, J., & Daisaka, H. 2011, PASJ, 63, 1331

Lacerda, P., & Luu, J. 2006, AJ, 131, 2314

Lawler, S. M., Pike, R. E., Kaib, N., et al. 2019, AJ, 157, 253

Lee, E. A., Astakhov, S. A., & Farrelly, D. 2007, MNRAS, 379, 229

Li, R., Youdin, A. N., & Simon, J. B. 2018, ApJ, 862, 14

Lin, H. W., Wu, Y. L., & Ip, W. H. 2007, AdSpR, 40, 238

Malhotra, R. 2019, GSL, 6, 12

Morbidelli, A., Tsiganis, K., Crida, A., Levison, H. F., & Gomes, R. 2007, AJ, 134, 1790

Morganson, E., Gruendl, R. A., Menanteau, F., et al. 2018, PASP, 130, 074501

Murray, C. D., & Dermott, S. F. 2000, Solar System Dynamics (Cambridge: Cambridge Univ. Press)

Murray, K., Holler, B. J., & Grundy, W. 2018, AAS/DPS Meeting, 50, 311.08

Nesvorný, D., Youdin, A. N., & Richardson, D. C. 2010, AJ, 140, 785

Noll, K., Grundy, W. M., Nesvorný, D., & Thirouin, A. 2020, in The Trans-Neptunian Solar System, ed. D. Prialnik, M. A. Barucci, & L. Young (Amsterdam: Elsevier), 201

Noviello, J. L., Desch, S. J., Neveu, M., Proudfoot, B. C. N., & Sonnett, S. 2022, PSJ, 3, 225

Ortiz, J. L., Thirouin, A., Campo Bagatin, A., et al. 2012, MNRAS, 419, 2315

Petit, J. M., Kavelaars, J. J., Gladman, B. J., et al. 2011, AJ, 142, 131

Rabinowitz, D. L., & Owainati, Y. 2014, AAS/DPS Meeting, 46, 510.07

Rabinowitz, D. L., Schaefer, B. E., & Tourtellotte, S. W. 2007, AJ, 133, 26

Roe, H. G., Pike, R. E., & Brown, M. E. 2008, Icar, 198, 459

Schlichting, H. E., & Sari, R. 2008, ApJ, 673, 1218

Showalter, M. R., Hamilton, D. P., Stern, S. A., et al. 2011, IAUC, 9221, 1

Showalter, M. R., Weaver, H. A., Stern, S. A., et al. 2012, IAUC, 9253, 1

Sicardy, B., Ortiz, J. L., Assafin, M., et al. 2011, Natur, 478, 493

Simon, J. B., Armitage, P. J., Youdin, A. N., & Li, R. 2017, ApJL, 847, L12

Spencer, D., Ragozzine, D., & Proudfoot, B. 2021, AAS/DPS Meeting, 53, 205.04

Szakáts, R., Kiss, C., Ortiz, J. L., et al. 2023, A&A, 669, L3

Tanga, P., Pauwels, T., Mignard, F., et al. 2022, arXiv:2206.05561

Thirouin, A., Noll, K. S., Ortiz, J. L., & Morales, N. 2014, A&A, 569, A3

Verbiscer, A. J., Helfenstein, P., Porter, S. B., et al. 2022, PSJ, 3, 95

Walsh, K. J., Morbidelli, A., Raymond, S. N., O'Brien, D. P., & Mandell, A. M. 2011, Natur, 475, 206

Weaver, H. A., Stern, S. A., Mutchler, M. J., et al. 2006, Natur, 439, 943

Weidenschilling, S. J. 2002, Icar, 160, 212

Youdin, A. N., & Goodman, J. 2005, ApJ, 620, 459